Evolution of Tantalum Content During Vacuum Induction Melting and Electroslag Remelting of a Novel Martensitic Steel

Martin Detrois[1,2,*], Paul D. Jablonski[1], Jeffrey A. Hawk[1]

[1] National Energy Technology Laboratory, 1450 Queen Ave. SW, Albany, OR 97321, USA
[2] Leidos Research Support Team, 626 Cochrans Mill Road, P.O. Box 10940, Pittsburgh, PA 15236, USA

* Corresponding author. *E-mail address:* martin.detrois@netl.doe.gov

Abstract

The need for materials with superior thermal and mechanical properties while mitigating cost increases interest in new complex alloy compositions which brings challenges to manufacturing processes. In this investigation, vacuum induction melting (VIM) and electroslag remelting (ESR) of a novel tantalum (Ta) containing martensitic steel was performed using standard industry practices at a laboratory scale. A 25% loss of Ta was measured from the VIM electrode to the ESR ingot using x-ray fluorescence. Several tools were used for broad characterization of the ingots, including LECO for chemistry analysis, scanning electron microscopy and electron probe microanalysis for observation of the precipitate and inclusion phases post-VIM and post-ESR as well as computational modeling of the ESR process for calculation of macrosegregation and inclusion travel. It was found that a significant amount of Ta_2O_5 inclusions formed during VIM and were transferred to the slag during ESR. While ESR was particularly successful at decreasing the number density of inclusions by 95%, additional efforts are needed with regards to vacuum leak rate and purity of stock material when melting novel advanced steels.

Keywords: Electroslag remelting, Vacuum induction melting, Slag, Tantalum, Oxide, Steel

I. Introduction

Electroslag remelting (ESR) is a widely used process to produce materials in which cleanliness is of upmost importance.[1] A consumable electrode is cast using vacuum induction melting (VIM) with a mold geometry optimized for ESR. The electrode is then placed in a water-cooled copper crucible that contains a ceramic slag (or flux) consisting of combinations of CaF_2, CaO, Al_2O_3, SiO_2 and MgO.[2] Although there are slags for general purpose melting such as 40-30-30 CaF_2-CaO-Al_2O_3, the slag composition can, and should, be optimized for electrical efficiency, prevention of Al pickup, and/or lubrication, among other factors. During ESR, electrical current passes from the electrode through the slag layer and forming ingot to the bottom of the crucible. The current superheats the electrically resistive slag which, in turn, causes the electrode to melt. Liquid metal droplets travel from the bottom of the electrode to the crucible where the ESR ingot forms. During their travel within the slag, the droplets are superheated which causes favorable reactions that (under usual circumstances) remove tramp elements.

Casting and remelting of metals have important features that lead to the production of final ingots that possess greater cleanliness with reduced segregation.[3] During VIM, the induction heating contributes to the motion of the liquid metal in the furnace crucible, resulting in a better mixing of the constituting elements of the alloy. Furthermore, removal of tramp elements such as oxygen is enabled during VIM by CO boil or in Cr-containing alloys where Cr-oxides form and float on top of the liquid metal or attach to the VIM skull.[4] During ESR, desulfurization of the liquid droplets occurs from their reaction with the CaO from the slag.[5]

Furthermore, ESR is particularly effective at removing inclusions that either dissolve or remain in the slag depending on their composition, size and density.[6]

Several factors influence the overall cleanliness of the final ingot and/or the efficiency of the removal of tramp elements and other undesirable inclusions during VIM and ESR. First, the selection of the melt stock is critical to the application intended for the alloy. Most alloys are made from industry-grade melt stock that contain impurities, such as oxygen, nitrogen and sulfur, usually in relatively high concentrations. For instance, Cr has an affinity for oxygen and selecting 500 ppm oxygen containing Cr versus 5000 ppm influences the cleanliness of the final product after melting. In some instances, industries use scrap metal to save on material cost, particularly for alloys that contain expensive elements such as Ni-based superalloys.[3] Another important factor is the atmosphere in which melting is performed, which is determined by pressure, leak rate and cover gas. In the VIM process, the integrity of the furnace is determined by the capability of the furnace to hold the pressure inside the chamber, and thus, prevent outside air from getting inside the furnace.[7] A large leak rate would result in oxygen and nitrogen being present around the liquid metal and decrease the cleanliness of the cast ingot.

After performing a leak check, pumping resumes until the furnace is backfilled with inert gas, most commonly argon (although this step is not always performed). Similarly, an argon atmosphere can be used during ESR to prevent oxygen and nitrogen from the air entering the melt[8]. Finally, selection of the melt parameters during ESR plays a role in reducing the amount of inclusions and/or tramp elements by controlling mixing in the slag and superheating of the liquid metal.[9] While the concentration of tramp elements can be decreased during melting, some of the material’s constituent elements can also be affected. The loss of reactive elements such as

Ti can occur during ESR from its reaction with the alumina (Al_2O_3) from the slag.[10] Similarly, pick up of Al in the liquid metal can occur when used as a deoxidizer for the slag.[11]

Consequently, it is essential to monitor and control the chemistry of manufactured alloys, particularly those with complex compositions and highly reactive elements. Recently, a novel advanced martensitic steel was designed, CPJ7[12], containing 15 elements of concentrations listed in Table I. Among them, highly reactive elements are present in narrow concentration ranges, namely Si, Nb and Ta. Tantalum is used in steels for the formation of carbides and carbonitrides such as MX precipitates that increase intergranular corrosion resistance and resistance to creep deformation. Tantalum is also used in Ni-based superalloys from 0 to above 10 wt.% for carbide formation, solution hardening and oxidation resistance.[13] Being an expensive alloying element with a strong affinity for oxygen (as well as hydrogen, nitrogen and carbon[14]), the concentration of Ta should be monitored during melting of novel alloys. The evolution of the concentration of Ta in VIM electrodes and ESR ingots of CPJ7 was studied in this investigation.

II. Experimental Procedure

Five CPJ7 alloys were considered in this investigation with heat designations Z, AA, AB, AC and AD, all with compositions within the range of Table I. The alloys were weighted to the target composition using commercial grade, high purity, melt stock with a total weight of 77 kg. The charges were loaded in an alumina crucible in a 136 kg capacity VIM furnace and ultra-high purity nitrogen and argon were backfilled to 200 Torr prior to starting the melt with the added nitrogen pressure determined to meet the chemistry requirements.[15] Once fully molten, the liquid was poured at approximately 50 K (50 °C) superheat with the liquidus temperature calculated from Thermo-Calc [16] using the Fe database. The liquidus temperature of the alloy was equal to 1763 K (1490 °C). The molds employed to form the ESR electrodes were steel cylinders with 114 mm inside diameter. Finally, leak rate checks were performed prior to each melt for 1 minute; the pressure at start, prior to backfilling the furnace was ~30 μHg with the leak rate around 6.5 μHg/min. Additional details on the typical VIM/ESR process used in the laboratory are described in Reference [9].

The ESR of the VIM ingot was performed after cropping the top and bottom of the ~114 mm diameter electrodes and welding a stub oriented so that the original top of the VIM ingot, which contains shrink, was first to melt. Melting was performed with ESR current control set to melt rate with a setpoint of 1.47 kg/min. Voltage control was set to voltage swing with a setpoint of 0.8 V in steady state. The slag was 40-30-30 CaF_2-CaO-Al_2O_3 with the detailed and complete chemistry listed in Table II. The slag was previously degassed in a steel retort under vacuum at 723 K (450 °C) for 1 h, followed by 793 K (520 °C) for 1 h, followed by 0.5 h at 1073 K (800 °C), using a ramp rate of 1 K/min (1 °C/min) between 793 K (520 °C) and 1073 K (800 °C).

The melts were started using compacts made of turnings of the VIM ingot layered with the slag at the bottom of a 152 mm diameter ESR crucible. Additional slag was added around the compact and in the feeder for startup. Each subsequent ingot was melted under an argon atmosphere protective cover. The run time for each electrode was approximately 52 min with steady-state conditions reached 13 min following startup. For more information about the startup process and operation of the ESR furnace used in this investigation, see Reference [17].

Specimens were extracted from the ESR ingots at various positions along the ingot for chemistry evaluation. The VIM ingot/ESR electrodes specimens were taken from a slice cut approximately 10 mm away from the bottom of the ingot while the chemistries of the ESR ingots were obtained from specimens extracted at the top of the ingot from an approximately 15 mm thick slice. The slag chemistry was analyzed by crushing the used slag (skin and cap) to fine particles and compacting into small specimens. X-ray fluorescence (XRF) was used to obtain the metal chemistries. A Rigaku ZSX Primus II was used with NIST traceable standards with reported values accurate to 0.01 wt.%. Trace and tramp element concentrations were determined using a LECO CS444LS for carbon and sulfur. A LECO TC436AR was used for oxygen and nitrogen concentrations, also using NIST traceable standards. Microstructural characterization was performed on the XRF samples following polishing to 0.05 μm using a solution of colloidal silica. The microstructures and various inclusions were observed on a FEI Inspect F field emission scanning electron microscope (SEM). An Oxford Instrument energy dispersive spectrometer (EDS) was used for preliminary phase identification. More detailed phase characterization was performed on a JEOL JXA-8530FPlus HyperProbe electron probe microanalyzer (EPMA).

Computational fluid dynamics (CFD) simulations of the ESR process were performed using MeltFlow-ESR from Innovative Research, LLC.[18] The thermo-physical properties of alloy CPJ7 were determined using JMatPro[19] and consisted, among others, of liquid and solid density, volume expansion coefficient, solidus and liquidus temperatures, latent heat, electrical conductivity and partitioning coefficient in addition to thermal conductivity, specific heat, viscosity and solid fraction as a function of temperature. Furthermore, inclusions were modeled using a range of relative densities and sizes, where the relative density was defined as the density of Ta_2O_5 over the liquid density of the alloy. Similarly, the slag thermo-physical parameters were used in the simulations and obtained from References [20] and [21]. The slag and metal properties are listed in Table III.

Finally, the melt parameters used in the simulations were those extracted from ESR experiments and consisted of the voltage setpoint, current setpoint and measured melt rate as a function of the melt time. The simulations were run using the dimensions of the electrode and crucible used in the laboratory as described in the second paragraph of Section II. Description of the model including the assumptions, boundary conditions and various governing equations used to model electromagnetics, fluid motion, phase change, inclusion behavior and macrosegregation, among others has been presented by Kelkar et al.[18,22].

Finally, the ESR ingots were sectioned into approximately 54 mm thick slices for hot working at 1273 K (1000 °C). The slices were first homogenized in a vacuum heat treatment furnace using a computationally optimized homogenization algorithm [23]. Hot working consisted of multiple forging steps to square the discs followed by hot rolling to form ~13 mm thick plates. The plates were then normalized at 1423 K (1150 °C) for 30 min followed by cooling in air. The plates were then aged at 973 K (700 °C) for 1 h followed by air cooling. This process was performed for weld testing experiments which are beyond the scope of this investigation. However, additional chemistry specimens for XRF and LECO analyses were extracted from the plates in locations corresponding to the centerline of the ingot, the mid-radius and outer radius to compare the results to the CFD predictions.

III. Results

The results of carbon, nitrogen, oxygen and sulfur concentrations in the electrode and ESR ingot product are presented in Figure 1 for the five heats Z, AA, AB, AC and AD. Both carbon and nitrogen contents were relatively unchanged from the VIM electrode to the ESR ingot with regard to the standard deviations and differences between the heats. A significant decrease in the oxygen content was observed for the five heats with a final concentration in the ESR ingots around 28 ppm. Thus, ESR of the CPJ7 electrodes resulted, on average, in a 49% decrease in oxygen content. Similarly, decreases in sulfur concentrations were found following ESR with a final amount around 10 ppm which represents, on average, a 56% decrease from the electrode to the resulting ESR ingot.

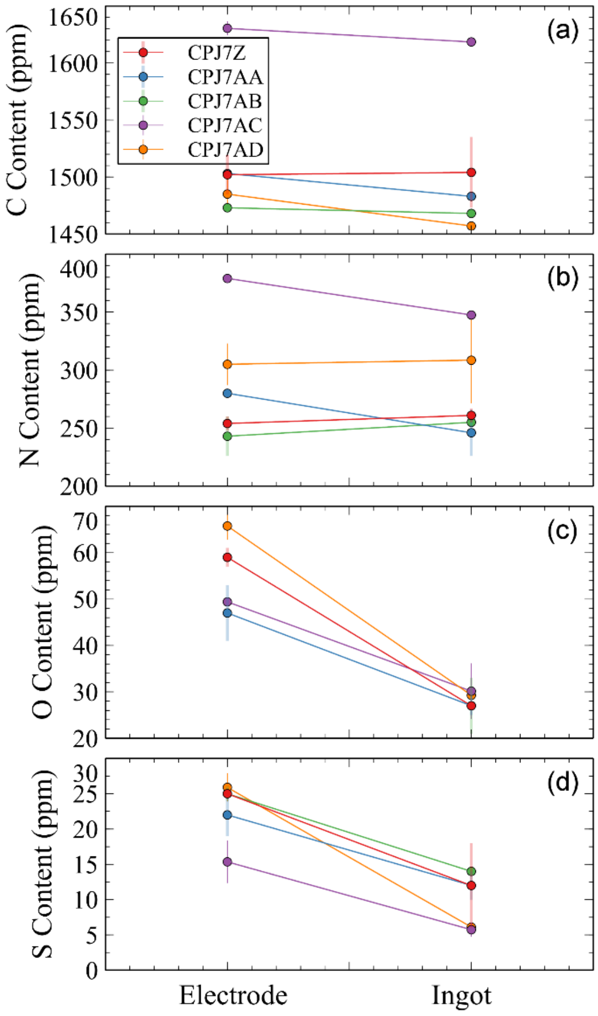

Fig. 1- (a) Carbon, (b) nitrogen, (c) oxygen and (d) sulfur concentrations before and after ESR for the five heats of CPJ7.

The XRF results of Ta concentrations revealed a relatively significant loss of Ta in the ESR ingot metal, and a gain of Ta in the slag after ESR, as observed in Figure 2. In CPJ7Z, the Ta concentration in the electrode and ingot almost spanned the entire Ta range specified in the composition of the alloy, Table I, with a starting concentration of 0.30 wt.% and final of 0.21 wt.% in the ESR ingot. Thus, the starting Ta concentration in the other two heats, CPJ7AA and CPJ7AB, was increased to obtain a Ta concentration in the ESR ingot more centered within the allowable range. In CPJ7AA, the Ta concentration decreased from 0.34 to 0.27 wt.% and from 0.33 to 0.25 wt.% in CPJ7AB. Similarly, the Ta concentration decreased from 0.33 to 0.25 wt.% and from 0.31 to 0.22 wt.% in CPJ7AC and CPJ7AD, respectively (not represented in Figure 2). On average, the decrease in Ta content in the metal was calculated at 25%. The opposite was observed in the slag where the Ta content in the virgin slag, prior to ESR, was below the detectable amount from XRF analysis (<0.001 wt.%). Following remelting, almost 2 wt.% Ta was measured in the used slag. From the chemistry for oxides reported in Table IV, 1.66 wt.% Ta_2O_5 was measured in the slag after ESR. MnO_2 and Cr_2O_3 were also detected. The concentration of CaF_2, CaO and MgO decreased and the Al_2O_3 content increased. Interestingly, a significant increase in the concentration of SiO_2 from 0.74 to 3.22 wt.% was also measured from XRF. This was associated with a decrease in the concentration of Si in the metal, as reported in Table V. On average, a 51% decrease in Si content was measured from ESR of the three CPJ7Z, CPJ7AA and CPJ7AB heats.

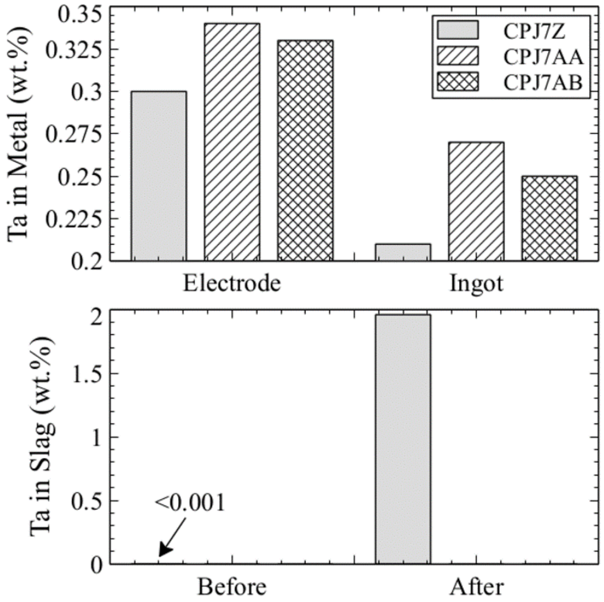

Fig. 2- Ta content in the metal from electrode to resulting ingot (i.e. before and after the ESR process) for three heats of CPJ7 and Ta content in the slag before and after ESR of CPJ7Z.

Observation of the microstructure of the CPJ7Z and CPJ7AC alloys in the SEM following VIM and ESR revealed two Ta-containing precipitate phases present after each melt sequence. The first was the interdendritic phase that commonly originates from elemental segregation during solidification, Figure 3. EPMA analysis revealed major partitioning of Ta and Nb, and less significant partitioning of Si, C and V. The phase was relatively depleted of Fe, Cr and, less significantly, of Co. The second phase was identified as Ta_2O_5 inclusions, Figure 4a. Relatively significant partitioning occurred for Si and V, with less partitioning for Mn and C (EPMA elemental maps of Figure 4b). Note that the Mn-rich region on the left of the inclusion of Figure 4b was identified as MnS.

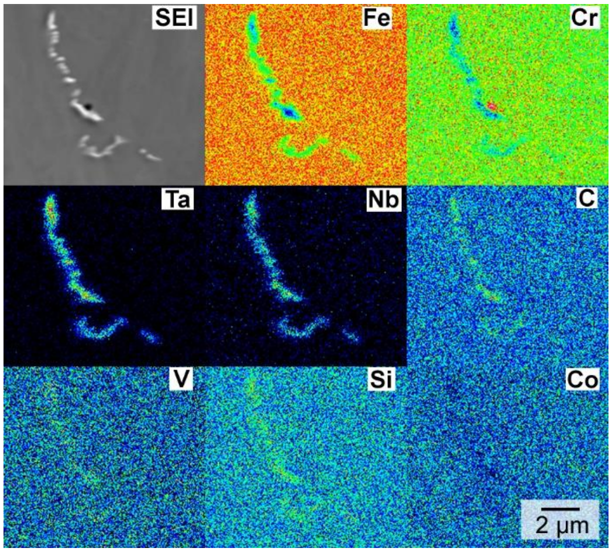

Fig. 3- EPMA elemental maps showing the interdendritic phase in CPJ7AC following VIM.

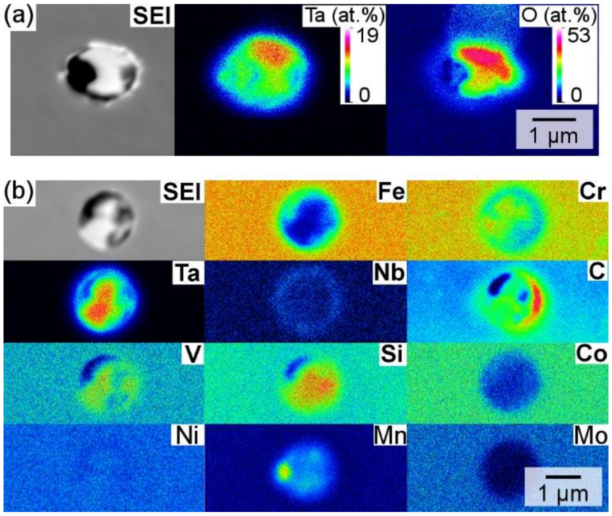

Fig. 4- EPMA elemental maps on Ta_2O_5 inclusions with (a) atomic percent concentration for Ta and O and (b) with the constituting elements of the alloy.

The interdendritic phase appeared throughout the microstructure and primarily at the grain boundaries. The precipitates appeared bright in the SEM (from the atomic number difference of Ta) and in the form of small plates as observed in Figure 5a. It should be noted that a brighter shadow can be observed on the SEM micrograph of Figure 5a which may be caused by elemental segregation as the alloy was not homogenized at that stage. While, the fraction and morphology of the interdendritic precipitates did not change visually from post-VIM to post-ESR condition, the area fraction was calculated and reported in Figure 5b for better accuracy. The results confirmed that no significant variation in the fraction of the precipitates occurred during ESR particularly considering the standard deviations over more than 10 regions similar to that of the SEM image in Figure 5a. The large standard deviations are attributed to the fine structure of the phase and its dependence on the grain size since the precipitates formed primarily at the grain boundaries and the cast structure is not homogeneous. Thus, the average fraction of the interdendritic phase in CPJ7Z and CPJ7AC was calculated at approximately 0.07%.

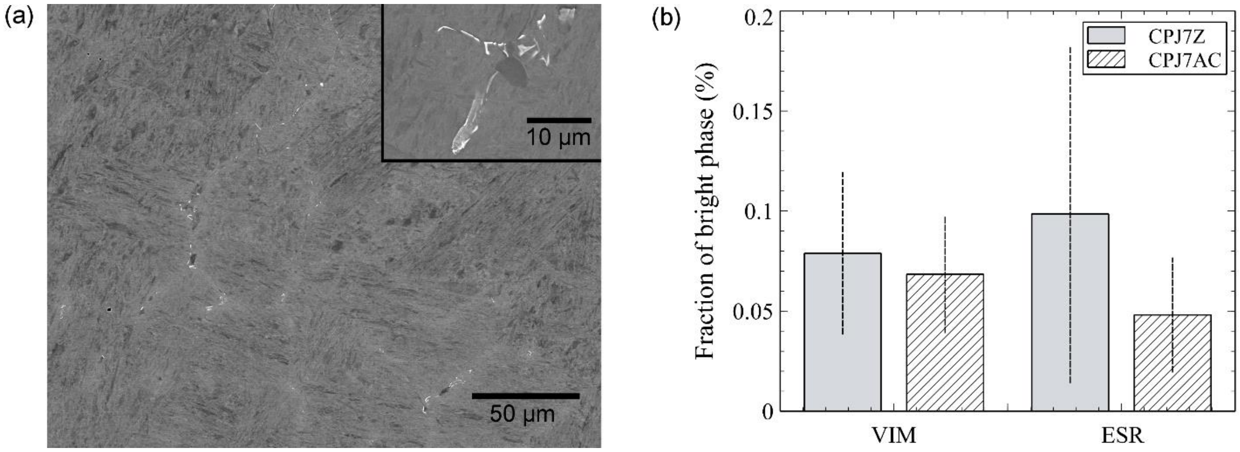

Fig. 5- (a) SEM images of the interdendritic phase found in the ESR electrode and resulting ingot with (b) calculated phase fraction from image analysis.

The second Ta-containing precipitate phase was found in the form of Ta_2O_5 inclusions, Figure 6a. On average, the number density of inclusions was calculated at 196 inclusions/mm^2 following VIM, Figure 6b, which represents an average of 11 inclusions on the SEM region of Figure 6a for visual reference. Following ESR, only 9 inclusions/mm^2 remained in the microstructure which represents an average of 0.5 inclusions in the surface of Figure 6a. Consequently, the ESR process resulted in a 95% reduction in the number density of inclusions in the CPJ7 alloy. The inclusions were measured to have an average diameter of 1.5 ± 0.6 µm.

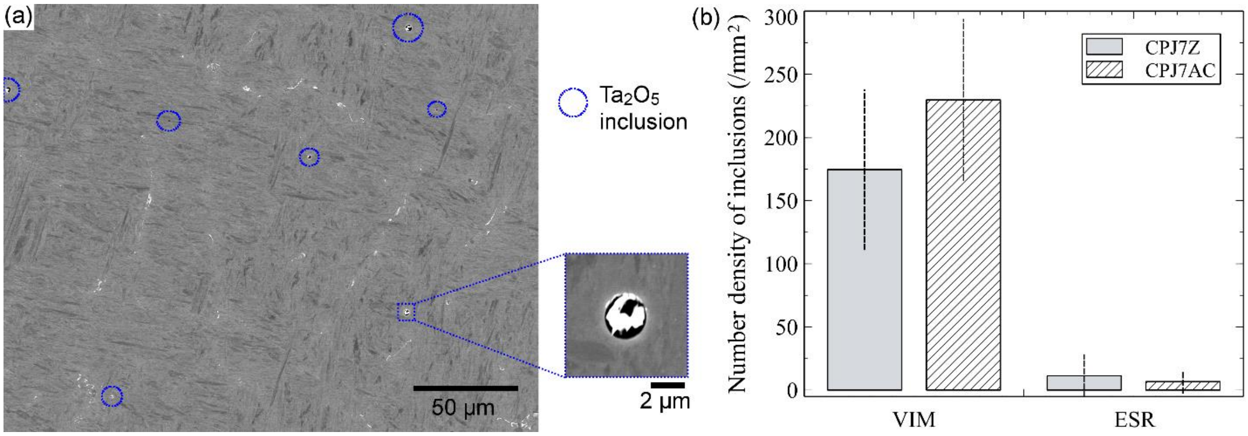

Fig. 6- (a) SEM images of inclusions found in the VIM ingots (i.e. ESR electrodes) and (b) calculated number density from image analysis following VIM and ESR for CPJ7Z and CPJ7AC.

The MeltFlow-ESR simulations were used to plot the predicted Ta content in CPJ7AC following ESR in Figure 7a. In this ingot, the concentration of Ta in the electrode was measured using XRF at 0.33 wt.% and this value was used as input in the simulations. The nominal (targeted) concentration of 0.33 wt.% is found in light blue between the center line and the outer radius. The lowest Ta content was found around the bottom of the ingot at approximately 0.29 wt.%. In the section of the ingot melted in steady state, the Ta content was higher around the centerline, above the nominal value, and decreased to below the nominal value at the outer radius. At X = 0.2 m for reference, the calculated Ta concentration was 0.35 wt.% at the centerline of the ingot (R = 0 m) and 0.32 wt.% at the outer radius.

A schematic of the sectioned ingot is represented in Figure 7b with the chemistry slice (A) used for XRF and LECO analyses and the various thick slices used for hot working to 13 mm thick plates. The Ta content from XRF analysis on the B, E and I plates was mapped in Figure 7c. First, the Ta content from XRF on the chemistry slice A was measured at 0.25 wt.%. Similar values were obtained at B0, B1, E0 and E1. The XRF-determined Ta concentration was found to decrease toward the outer radius to 0.237 wt.% at B2 and 0.238 wt.% at E2, and more so towards the bottom of the ingot with values of 0.215, 0.219 and 0.207 wt.% at I0, I1 and I2, respectively. Note that the variations in Ta content recorded on the XRF throughout the radius of the ingot are only relevant with an added significant figure when compared to those from the MeltFlow-ESR simulations.

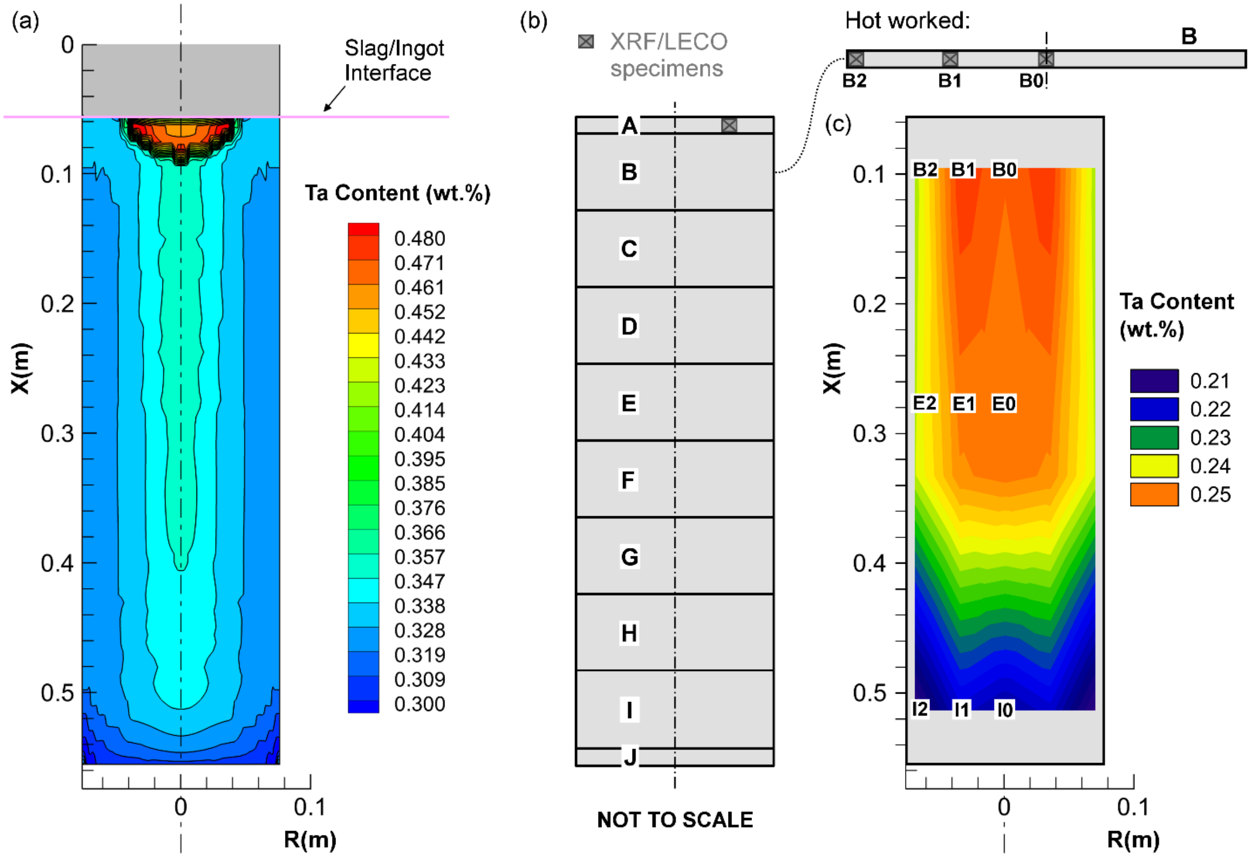

Fig. 7- (a) MeltFlow-ESR predicted Ta concentration throughout the solidified ingot in CPJ7AC, (b) schematic of the ingot cut into slices for hot working with the resulting plates for chemistry specimens and (c) XRF measured Ta concentration obtained at three times three locations in the ingot CPJ7AC (slices B, E and I).

IV. Discussion

A 25% decrease in the Ta content of martensitic steel CPJ7 was observed from VIM to ESR in ingots prepared using standard industry practices. Tantalum is used in CPJ7 primarily to form the MX precipitate phase and improve resistance to creep deformation. In the cast condition, the interdendritic phase was observed in Figures 3 and 5a and its presence resulted from the segregation of reactive elements, particularly Ta and Si. The interdendritic phase is dissolved later after the alloy undergoes the homogenization heat treatment cycle, while the MX phase forms during subsequent aging. The morphology of the interdendritic phase did not visually change after ESR as well as its calculated fraction (see Figure 5b). Thus, the interdendritic phase does not influence the overall Ta concentration measurements for the alloys particularly considering the use of XRF (large sampling area). Therefore, from the results presented, it is evident that the strong presence of Ta_2O_5 inclusions following VIM and the 95% decrease in number density of said inclusions during ESR is the main reason for the decrease in concentration of Ta in the ingot and increase in the slag during ESR.

Prior to starting the melt in the 136 kg capacity VIM furnace, the chamber was pumped down to approximately 30 μHg pressure. A leak rate test over a one-minute time range was systematically performed before backfilling to the desired nitrogen pressure (that leads to the N concentration in the alloy) and 200 torr argon gas. On average, the leak rates were approximately 6.5 μHg/min which is acceptable in the industry. Thus, some oxygen is expected to originate from outside air, but the amount should be relatively limited. Another source of oxygen, however, is the raw Cr which contains 5000 ppm O. With 10 wt.% Cr in the CPJ7 alloys, 500 ppm O is already present in the melt charge, originating from the raw Cr only. Therefore, with oxygen concentrations in the electrode between 40 and 70 ppm following VIM, the VIM process was particularly effective at removing oxygen from the melt, Figure 1. While this can be attributed to oxides floating on top of the liquid metal during VIM or attaching to the VIM skull (particularly Cr-oxides), some of the oxygen reacted with Ta to form Ta_2O_5 inclusions, Figures 4 and 6a.

To compare the influence of the leak rate and raw Cr on the oxygen content and amount of Ta_2O_5 inclusions following VIM, two smaller CPJ7 melts were performed in a 9 kg capacity VIM furnace that has a sub-micron leak rate. The findings after melting are reported in Table VI. In the first melt, the leak rate was measured at 0.73 μHg/min. When using 5000 ppm O containing Cr, the measured oxygen content in the VIM ingot from LECO analysis was 74 ppm which is close to that measured in the large CPJ7 VIM ingots. SEM analysis further revealed the presence of Ta_2O_5 inclusions with a number density of 111 inclusions/mm^2, which is less than the results contained in Figure 6. This suggests that the lower leak rate was beneficial in preventing Ta_2O_5 formation.

In the second melt, the leak rate measured was comparable at 0.34 μHg/min and a higher-grade Cr was used (400 ppm O). LECO analysis revealed 105 ppm O concentration in the VIM ingot following melting while SEM analysis showed a density of inclusions of 136 inclusions/mm^2. Thus, it might be necessary to use even higher purity melt stock to prevent the formation of the Ta-oxides. It should be noted that the oxygen content from the 9 kg furnace ingots were higher than from the 136 kg furnace. This may be attributed to the different location were specimens were extracted for analysis (bottom of large heat and top of small heats). Furthermore, oxygen can originate from other elements (not tracked or discussed).

The removal of inclusions during ESR is primarily driven by their absorption and dissolution in the slag[24] while some travel in the moving fluid.[25,26] Mixing in the slag originates from the slag losing heat from both the melting electrode and the water-cooled copper crucible, as observed on the temperature gradient of Figure 8 at X = 0 m and R = 0.076 m in the slag (described in Reference [27]). This creates two flow loops in the simulations described in Figure 8 that can be identified from the liquid direction in the slag. For inclusions traveling in the slag, the model describes the inclusion trajectories assuming no dissolution and by introducing them under the slag/metal interface from the center (R = 0 m) to R = 0.057 m, the radius of the electrode. It was found in Figure 8 that, due to their relative density and sizes, most inclusions travelled around the center loop, below the electrode, while some travelled around the outer loop. Few trajectories were predicted to enter the liquid metal in the mushy zone, adding to the non-complete removal of inclusions observed in Figure 6b. It should be noted that the decrease in oxygen from VIM to ESR observed in Figure 1c correlates to the removal of inclusions from the VIM electrode.

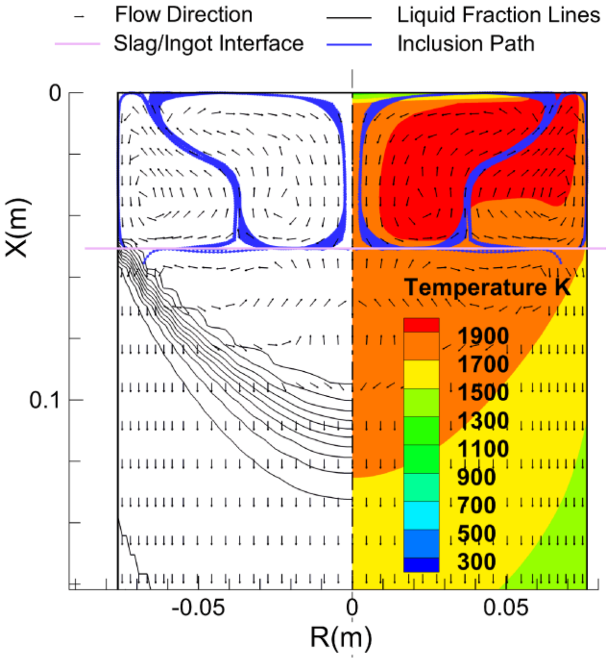

Fig. 8- MeltFlow-ESR simulation of Ta_2O_5 inclusion travel during ESR of CPJ7AC for a range of relative densities ρ_r (0.8, 0.9, 1, 1.1 and 1.2ρ_r) and a 1 μm particle size with flow direction, liquid fraction lines and temperature gradient in the slag, sump and solidified ingot.

The macrosegregation observed in Figure 7 is a known product of ESR and has been described for Nb in Alloy 625 by Fezi et al.[28]. During solidification of the liquid metal, the interdendritic liquid becomes enriched with Ta due to its partitioning coefficient respective to the bulk composition. The liquid motion in the sump causes the interdendritic front to move towards the ingot centerline and limits its travel towards the outer radius, since liquid motion is weaker in the center of the molten metal pool, and eventually creates the radial variations observed in Figure 7a. The longitudinal variations are attributed to the enrichment in Ta of the melt pool throughout the melt, and thus, throughout solidification of the ingot thereby causing a slight increase in concentration from bottom to top, as described by Kelkar et al.[18]. The partitioning predicted in Figure 7a is confirmed experimentally on part of the ingot in Figure 7c. The trends between computational and experimental results agree, while the differences in values are attributed to the overall Ta loss from the removal of inclusions not captured with respect to elemental concentration in the simulations. It should be noted that the macrosegregation observed in Figure 7 can influence the calculation of the Ta loss from the removal of inclusions depending on the location of the XRF specimens. However, the losses presented in the results section, and in Figure 2, were calculated using specimens extracted from slice A (Figure 7b) in consistent locations and that were shown to present Ta concentrations representative of the centerline up to mid-radius of the ESR ingot, on the higher end of the concentration range, which mitigates the influence of macrosegregation.

Although the Ta loss from VIM to ESR is attributed to the removal of the Ta_2O_5 inclusions, possible reactions may have occurred between the liquid metal and slag during ESR thereby contributing to the variation in Ta content. The simplified Ellingham diagram for selected oxides is shown in Figure 9 using the data from Reference [29]. While falling above some of the slag constituents on the diagram, Ta_2O_5 is a very stable oxide, along with SiO_2 and TiO_2. As reported in Figure 4b, the Ta_2O_5 inclusions show strong partitioning of Si and the slag composition following ESR showed elevated concentrations of not only Ta_2O_5 but also SiO_2, Table IV. It is common for certain slags to contain SiO_2, particularly for remelting of steels as it improves lubrication and leads to a better ingot surface quality.[30] However, the authors also underlined the possible reaction between SiO_2 and highly reactive elements such as Al and Ti to explain why SiO_2 containing slags are avoided during ESR of Ni-based superalloys. The following reaction exists between Ta and SiO_2 in a slag-iron system[31]:

$$4[Ta] + 5(SiO_2) = 2(Ta_2O_5) + 5[Si] \qquad (1)$$

From the reaction of Eq. 1, the Ta in the electrode could have oxidized due to SiO_2 from the slag, however, the reaction would only be possible when enough SiO_2 is also transferred to the slag from dissolution of the inclusions. Therefore, this reaction is unlikely to have contributed to the loss of Ta, particularly considering the low concentration of SiO_2 in the slag chemistry, Table II, and the loss of Si in the metal, Table V. Another factor potentially influencing Ta loss remains the potential oxidation of Ta by the slag constituents. Alumina is a primary suspect as an increase in the Al concentration was measured in the metal before and after ESR from 90 to 140 ppm. Similar to the reaction of Al_2O_3 with Ti in superalloys,[32] the reaction of Ta and Al_2O_3 can be expressed as follow:

$$6[Ta] + 5(Al_2O_3) = 3(Ta_2O_5) + 10[Al] \qquad (2)$$

It should be noted that a similar reaction could take place between Si and Al_2O_3 as described by Shi et al.[33] which can also account for the increased Al content in the metal following ESR:

$$3[Si] + 2(Al_2O_3) = 3(SiO_2) + 4[Al] \qquad (3)$$

However, the contributions of Equation 2 to the loss of Ta is expected to be far less than that of the inclusion removal with regards to the decrease in oxygen content from VIM to ESR (Figure 1) and increase in Al_2O_3 in the slag. Nevertheless, more research is needed to assess oxidation of Ta during ESR particularly as a function of slag chemistry. This will require electrodes with few Ta_2O_5 inclusions to reduce the number of variables which, according to the Ellingham diagram, will be challenging as Ta_2O_5 is more stable than Cr_2O_3, illustrating the difficulty of avoiding Ta-oxide inclusion formation during VIM.

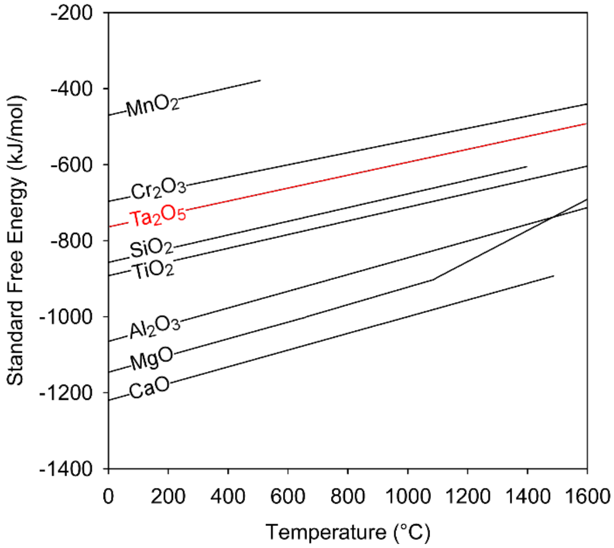

Fig. 9- Ellingham diagram for select oxides. Data extracted from Reference [29].

V. Conclusions

Vacuum induction melting and electroslag remelting of a novel Ta-containing martensitic steel were performed to study the evolution of Ta throughout the process. The following conclusions are reported:

1. The Ta content in CPJ7 decreased by 25% during ESR which was attributed to the formation of Ta_2O_5 inclusions during VIM and subsequent 95% reduction in number density of inclusions during ESR.
2. Ta is a highly reactive element and is prone to the formation of Ta_2O_5 oxides during VIM when the selected melt stock contains significant amounts of oxygen. Tantalum oxide formation in this investigation was slightly influenced by the leak rate, more so than the starting pressure during VIM for a leak rate range from sub-micron to ~10 μHg/min and a pressure range from around 0.04 to 50 μHg.

3. Macrosegregation of Ta was predicted from CFD-based simulations and confirmed experimentally using XRF measurements. The Ta concentration was higher at the centerline of the ESR ingot and decreased towards the outer radius and the bottom of the ingot.
4. The fraction and morphology of the Ta-containing interdendritic phase forming during solidification from elemental segregation did not significantly change from the VIM to the ESR condition.

Acknowledgements

This work was performed in support of the US Department of Energy's Fossil Energy Crosscutting Technology Research Program. The Research was executed through the NETL Research and Innovation Center's Advanced Alloy Development Field Work Proposal. Research performed by Leidos Research Support Team staff was conducted under the RSS contract 89243318CFE000003. The authors would like to thank Mr. Edward Argetsinger and Mr. Joseph Mendenhall for assistance in melting, Mr. Richard Chinn for XRF analysis, Mr. Peter Hsieh and Mr. Christopher McKaig for LECO analysis, Mr. Matthew Fortner for metallographic preparation and Mr. Keith Collins for EPMA. The authors would also like to thank Kanchan M. Kelkar from Innovative Research LLC and Krzysztof Wroblewski from American Flux & Metal LLC for the useful discussions.

Disclaimer

This project was funded by the Department of Energy, National Energy Technology Laboratory, an agency of the United States Government, through a support contract with Leidos Research Support Team (LRST). Neither the United States Government nor any agency thereof, nor any of their employees, nor LRST, nor any of their employees, makes any warranty, expressed or implied, or assumes any legal liability or responsibility for the accuracy, completeness, or usefulness of any information, apparatus, product, or process disclosed, or represents that its use would not infringe privately owned rights. Reference herein to any specific commercial product, process, or service by trade name, trademark, manufacturer, or otherwise, does not necessarily constitute or imply its endorsement, recommendation, or favoring by the United States Government or any agency thereof. The views and opinions of authors expressed herein do not necessarily state or reflect those of the United States Government or any agency thereof.

References

1 G. Hoyles: *Electroslag Processes: Principles and Practice*, Applied Science Publishers Co., Inc., New York, 1983.

2 A. Mitchell: in *LMPC 2005 - Proceedings of the 2005 International Symposium on Liquid Metal Processing and Casting*, P.D. Lee, ed., ASM International, Materials Park, Ohio, USA, 2005, pp. 195–200.

3 G.E. Maurer and A.D. Patel: in *LMPC 2005 - Proceedings of the 2005 International Symposium on Liquid Metal Processing and Casting*, ASM International, Materials Park, Ohio, USA, 2005.

4 F.N. Darmara: *JOM*, 1967, vol. 19, pp. 42–8. DOI: 10.1007/BF03378664

5 D. Hou, Z.-H. Jiang, Y.-W. Dong, Y. Li, W. Gong, and F.-B. Liu: *Metall. Mater. Trans. B*, 2017, vol. 48, pp. 1885–97. DOI: 10.1007/s11663-017-0921-0

6 M. Detrois and P.D. Jablonski: in *LMPC 2017: Proceedings of the Liquid Metal Processing & Casting Conference 2017*, M.J.M. Krane, R.M. Ward, S. Rudoler, A.J. Elliott, and A. Patel, eds., TMS, Philadelphia, PA, 2017, pp. 75–84. DOI: 10.2172/1406915

7 ASM: in *ASM Handbook, Volume 15: Casting*, ASM International, Materials Park, Ohio, USA, 2008, pp. 1–8.

8 C. Shi, X. Chen, and H. Guo: *Int. J. Miner. Metall. Mater.*, 2012, vol. 19, pp. 295–302. DOI: 10.1007/s12613-012-0554-x

9 M. Detrois and P.D. Jablonski: in *Proceedings of the 9th International Symposium on Superalloy 718 & Derivatives: Energy, Aerospace, and Industrial Applications*, E. Ott, X. Liu, J. Andersson, Z. Bi, K. Bockenstedt, I. Dempster, J. Groh, K. Heck, P.D. Jablonski, M. Kaplan, D. Nagahama, and C. Sudbrack, eds., Springer International Publishing, Pittsburgh, PA, 2018, pp. 287–302. DOI: 10.1007/978-3-319-89480-5_17

10 T.R. Bandyopadhyay, P.K. Rao, and N. Prabhu: *Metall. Min. Ind.*, 2012, vol. 4, pp. 6–16.

11 B. Arh, B. Podgornik, and J. Burja: *Mater. Tehnol.*, 2016, vol. 50, pp. 971–9. DOI: 10.17222/mit.2016.108

12 US9556503B1: 2017.

13 A. Choudhury: *ISIJ Int.*, 1992, vol. 32, pp. 563–74. DOI: 10.2355/isijinternational.32.563

14 W. Köck and P. Paschen: *JOM*, 1989, vol. 41, pp. 33–9. DOI: 10.1007/BF03220360

15 P.D. Jablonski and J.A. Hawk: in *Proceedings of the 2013 International Symposium on Liquid Metal Processing & Casting*, M.J.M. Krane, A. Jardy, R.L. Williamson, and J.J. Beaman, eds., Springer International Publishing, Cham, 2013, pp. 315–9. DOI: 10.1007/978-3-319-48102-9_45

16 J.O. Andersson, T. Helander, L. Höglund, P. Shi, and B. Sundman: *Calphad Comput. Coupling Phase Diagrams Thermochem.*, 2002, vol. 26, pp. 273–312. DOI: 10.1016/S0364-5916(02)00037-8

17 P.D. Jablonski, M. Cretu, and J. Nauman: in *LMPC 2017: Proceedings of the Liquid Metal Processing & Casting Conference 2017*, M.J.M. Krane, R.M. Ward, S. Rudoler, A.J. Elliott, and A. Patel, eds., TMS, Philadelphia, PA, 2017, pp. 157–62.

18 K.M. Kelkar, S. V. Patankar, S.K. Srivatsa, R.S. Minisandram, D.G. Evans, J.J. DeBarbadillo, R.H. Smith, R.C. Helmink, A. Mitchell, and H.A. Sizek: in *Proceedings of the 2013 International Symposium on Liquid Metal Processing & Casting*, M.J.M. Krane, A. Jardy, R.L. Williamson, and J.J. Beaman, eds., Springer, Cham, 2013, pp. 3–12. DOI: 10.1007/978-3-319-48102-9_1

19 N. Saunders, Z. Guo, X. Li, A.P. Miodownik, and J.P. Schillé: *Jom*, 2003, vol. 55, pp. 60–5. DOI: 10.1007/s11837-003-0013-2

20 D.D. Gohil and K.C. Mills: *Arch. für das Eisenhüttenwes.*, 1981, vol. 52, pp. 335–40. DOI: 10.1002/srin.198104944

21 B. Birol, G. Polat, and M.N. Saridede: *JOM*, 2015, vol. 67, pp. 427–35. DOI: 10.1007/s11837-014-1230-6

22 K.M. Kelkar, S. V. Patankar, and A. Mitchell: in *LMPC 2005: Proceedings of the 2005 International Symposium on Liquid Metal Processing and Casting*, 2005, pp. 1–8. http://inresllc.com/assets/files/meltflow/ESR-Model_LMPC-2005-Conference.pdf

23 P.D. Jablonski and J.A. Hawk: *J. Mater. Eng. Perform.*, 2017, vol. 26, pp. 4–13. DOI:

10.1007/s11665-016-2451-3

24 Y. Dong, Z. Jiang, Y. Cao, A. Yu, and D. Hou: *Metall. Mater. Trans. B*, 2014, vol. 45, pp. 1315–24. DOI: 10.1007/s11663-014-0070-7

25 Q. Wang, R. Wang, Z. He, G. Li, B. Li, and H. Li: *Int. J. Heat Mass Transf.*, 2018, vol. 125, pp. 1333-44. DOI: 10.1016/j.ijheatmasstransfer.2018.04.168

26 X. Huang, B. Li, Z. Liu, X. Li, and M. Sun: *Metals (Basel).*, 2018, vol. 8, p. 392. DOI: 10.3390/met8060392

27 A.S. Ballantyne: in *LMPC 2017: Proceedings of the Liquid Metal Processing & Casting Conference 2017*, M.J.M. Krane, R.M. Ward, S. Rudoler, A.J. Elliott, and A. Patel, eds., TMS, Philadelphia, PA, 2017, pp. 177–82.

28 K. Fezi, J. Yanke, and M.J.M. Krane: *Metall. Mater. Trans. B Process Metall. Mater. Process. Sci.*, 2015, vol. 46, pp. 766–79. DOI: 10.1007/s11663-014-0254-1

29 U. of Cambridge: DoITPoMS Ellingham Diagrams.

30 C. Bin Shi, J. Li, J.W. Cho, F. Jiang, and I.H. Jung: *Metall. Mater. Trans. B Process Metall. Mater. Process. Sci.*, 2015, vol. 46, pp. 2110–20. DOI: 10.1007/s11663-015-0402-2

31 Q. Han, J. Deng, S. Huang, and Y. Fang: *Metall. Trans. B*, 1990, vol. 21, pp. 873–8. DOI: 10.1007/BF02657813

32 Z. Jiang, D. Hou, Y. Dong, Y.-L. Cao, H. Cao, and W. Gong: *Metall. Mater. Trans. B*, 2016, vol. 47, pp. 1465–74. DOI: 10.1007/s11663-015-0530-8

33 C. Shi, H. Wang, and J. Li: *Metall. Mater. Trans. B*, 2018, vol. 49, pp. 1675–89. DOI: 10.1007/s11663-018-1296-6

Table I. Composition Range of the CPJ7 Martensitic Steel Investigated with Fe Balanced (Wt. Pct)[12]

	Cr	Mo	C	Mn	Si	Ni	V	Nb	N	W	Co	Ta	Cu	B
Min.	9.75	1.0	0.13	0.25	0.08	0.15	0.15	0.05	0.015	0.25	1.35	0.20	0.003	0.0070
Max.	10.25	1.5	0.17	0.50	0.15	0.30	0.25	0.08	0.035	0.75	1.65	0.30	0.30	0.0110

Table II. Slag Chemistry from Vendor (Wt. Pct)

CaF_2	CaO	MgO	Al_2O_3	SiO_2	C	S	MnO_2	Fe	TiO_2	P	LOI
38.94	31.50	0.691	28.81	0.16	0.001	0.013	0.006	0.054	0.102	<0.01	0.036

Table III. Thermo-Physical Parameters Used in the Simulations

	Slag	Metal
Liquid Density	2.67×10^3 kg/m^3	7.11×10^3 kg/m^3
Solid Density	2.90×10^3 kg/m^3	7.46×10^3 kg/m^3
Volume Expansion Coefficient (Liquid)	1.30×10^{-4} /K	4.13×10^{-5} /K
Solidus Temperature	1587 K (1314 °C)	1468 K (1195°C)
Liquidus Temperature	1673 K (1400 °C)	1763 K (1490°C)
Latent Heat	4.30×10^5 J/kg	1.85×10^5 J/kg
Electrical Conductivity (Liquid)	1.82×10^2 /Ω-m	8.72×10^5 /Ω-m
Thermal Conductivity (Liquid)*	0.5 W/m-K	38.7 W/m-K
Specific Heat (Liquid)*	1.23×10^3 J/kg-K	7.96×10^2 J/kg-K
Viscosity (Liquid)*	3.90×10^{-2} kg/m-s	7.10×10^{-3} kg/m-s
Emissivity	0.90	-

*Additional values were used as a function of temperature

Table IV. Concentration of Specific Oxides in the Slag Before and After ESR of CPJ7Z from XRF (Wt. Pct)

	CaF_2	CaO	MgO	Al_2O_3	SiO_2	MnO_2	TiO_2	Ta_2O_5	Cr_2O_3
Before	53.28	27.50	0.58	17.20	0.74	-	-	-	-
After	48.49	26.26	0.42	18.75	3.22	0.14	-	1.66	0.35

Table V. Concentration of Si in the Metal and Slag Before and After ESR from XRF (Wt. Pct)

		CPJ7Z	CPJ7AA	CPJ7AB
Metal	Before	0.09	0.10	0.08
	After	0.04	0.06	0.04
Slag	Before	0.41	-	-
	After	1.79	-	-

Table VI. Oxygen Content and Inclusion Density Following VIM of CPJ7 Ingots Under Various Conditions

Furnace	Charge Weight (kg)	O Content in Cr (ppm)	Pressure at Start (μHg)	Leak Rate (μHg/min)	O Content (ppm)	Number Density of Inclusions (mm^{-2})
136 kg*	77	~5000	29.6 ± 8.7	6.5 ± 1.9	56 ± 8	196 ± 67
9 kg	7	~5000	0.042	0.73	74 ± 13	111 ± 41
	7	~400	0.028	0.34	105 ± 5	136 ± 41

* Average between the ingots Z, AA, AB, AC and AD with standard deviations.